Focal mechanisms of small earthquakes beneath the Japanese islands based on first-motion polarities picked using deep learning

Takahiko Uchide[1,*]

[1] Geological Survey of Japan, National Institute of Advanced Industrial Science and Technology (AIST)

Abbreviated Title: Focal Mechanisms in the entire Japanese islands

* Corresponding Author: Takahiko Uchide (t.uchide@aist.go.jp)

Summary

Knowledge of crustal stress fields is essential for understanding tectonics and earthquake generation. One approach for estimating the crustal stress field is based on the focal mechanisms of earthquakes. This study investigated the focal mechanisms of approximately 110,000 microearthquakes in the area of the Japanese islands that occurred at a depth shallower than 20 km, based on the first-motion polarities picked by a simple neural network model. The model was first trained using a data set of mainly moderate to large earthquakes throughout Japan. Following on, the model was re-trained using a data set of microearthquakes in two regions of Japan. The threshold of the confidence score from the neural network model was chosen to maximize the overall quality of the focal mechanism solutions. The P- and T-axes of the numerous focal mechanism solutions provided more detailed distributions of the crustal stress field. For example, in the Chugoku region, small differences were observed in the trend of P-axes azimuths between the northern and southern areas, spatially corresponding to geodetic observations. The results of this study are useful for revealing the crustal stress field, and, as such, for assessing past and current tectonic activities and potential future earthquake generation.

Keywords

- Earthquake source observations
- Seismicity and tectonics
- Neural networks, fuzzy logic

1. Introduction

Crustal stress field data is crucial for understanding tectonics and seismic activity; however, measuring the stress at depths over a large area is challenging. Direct measurements at specific boreholes (e.g., Wu *et al.* 2007; Huffman *et al.* 2016; Brodsky *et al.* 2017; Townend *et al.* 2017) offer detailed information but only as it concerns one spot. In contrast, seismology provides indirect measurements for a wider area but includes more uncertainty. The focal mechanisms, which indicate the fault plane and slip directions, specify the orientation of seismogenic stress. The World Stress Map (Heidbach *et al.* 2008, 2016, 2018) presents the global compilation of this information.

In the past, routinely determined moment tensor solutions were used for estimating regional stress fields (Terakawa and Matsu'ura 2010; Hardebeck 2015). However, non-estimated areas remain, even in seismically active areas such as the Japanese islands. More complete knowledge of the seismogenic stress field requires focal mechanisms for microearthquakes, particularly in low seismicity areas (e.g., Imanishi *et al.* 2011, 2012; Matsumoto *et al.* 2015). Comprehensive investigations of microearthquake focal mechanisms contributed to revealing the regional stress field (e.g., Iio *et al.* 2018; Imanishi *et al.* 2019).

The focal mechanisms of moderate or larger earthquakes can be automatically determined using the full waveform from the local (e.g., Dreger and Helmberger 1993; Fukuyama *et al.* 1998) or global (e.g., Ekström et al. 2012) seismic network. However, the mechanisms of small earthquakes cannot be similarly determined due to the difficulty of modeling high-frequency seismograms. Instead, the first-motion polarity is typically used in this regard, where the vertical component initially moves either upward or

downward. Automatic polarity-picking methods include an approach based on the sign of the first extremum after the P arrival (Nakamura 2004; Chen and Holland 2016). Pugh et al. (2016a) proposed a Bayesian approach using the first extremum and a probability function of P arrival time. Recently, deep learning allowed for automatically picking the polarity (Ross *et al.* 2018; Hara *et al.* 2019). Deep learning has the approximation capabilities of a multilayer neural network to arbitrary functions (Hornik 1991). This presents an advantage in the polarity-picking problem, which involves the polarity of the first pulse and the various forms of seismic noise.

This study aimed to obtain focal mechanism solutions for the Japanese islands, one of the most seismically active regions in the world. The first-motion polarities were picked using a neural network model and seismic data from nationwide seismic networks. Finally, the focal mechanism solutions and spatial trends in P- and T-axes were reviewed.

2. Training the Neural Network Model

2.1. Design of the Neural Network Model

Fig. 1 summarizes the neural network used in this study. The input of the neural network model was a 256-sample-long seismogram in which the 156th sample corresponded to the P-arrival time already picked either manually or automatically. The output comprised two scores (confidence scores) corresponding to the upward and downward polarities. Note that, in the case of Southern California, Ross et al. (2018) classified the polarity as “up,” “down,” and “unknown”; however, in this study, the “unknown” class was not set. The data set included many seismograms with impulsive onset but no polarity information (Fig. 2), and the lack of polarity information did not

indicate "unknown" in this case. Thus, no training data set was available for the "unknown" class and such a class could not be set for the present study. In the cases with first-motion polarities being ambiguous, the confidence scores for both polarities are expected to have similar values. A confidence threshold was set for this research at a subsequent stage to accept suggested polarity information for determining the focal mechanism.

A simple neural network model (Fig. 1) similar to those used in prior studies (Ross *et al.* 2018; Hara *et al.* 2019) was designed. The neural network model started with two convolution layers, followed by three units comprising convolution, batch normalization (Ioffe and Szegedy 2015), and the maximum pooling layers. The model ended with two fully connected layers. The kernel size of the convolutional layers was 11. For all but the final layers, the activation function was the rectified linear units (known as "ReLU") (Nair and Hinton 2010); the SoftMax function was chosen for the final layer:

$$\mathrm{softmax}(\mathbf{z})_i = \frac{\exp(z_i)}{\sum_j \exp(z_j)}, \qquad (1)$$

where $\mathbf{z} = (z_1, z_2)$ is the output of the final layer corresponding to the upward and downward polarities, respectively. The final outputs (confidence scores) are non-negative and their summation is always 1.

2.2. Training Procedure

Generally, the training of neural network models requires training, validation, and test data sets. In this study, the data sets comprised the seismograms and the polarity. The training data set was used for optimizing the parameters in the neural network model. The initial values of the model parameters were randomly set. The negative log-likelihood

function was employed as a loss function to quantify the difference between the output of the model and the polarity expectation from the training data set, i.e., (1, 0) for the upward polarity and (0, 1) for the downward polarity. The value of the loss function was simply called a loss. The parameters of the neural network model were updated by back-propagating the loss (Rumelhart et al. 1986) optimized by the adaptive moment estimation (known as "Adam") method (Kingma and Ba 2014). This optimization was iteratively performed to decrease the loss.

The problem to be carefully addressed is the overfitting problem that the trained model works well with the training data but poorly with unseen data. This study addressed the overfitting problem in two ways. One was by using the dropout technique (Srivastava et al. 2014), where 50% of randomly selected perceptions were muted during the training. The second approach involved performing cross-validation using a validation data set that was independent of the training set. If the loss for the validation data set increased as the training progressed, while that for the training data set decreased for 10 iterations (epochs), the training was stopped.

Following the completion of the training, the performance of the trained model was examined using another data set (test data set) of small to microearthquakes, as the present study focused on such small events.

Since the data set of microearthquakes available in this study was small, training of the neural network model was performed in two stages. In the first stage, training was carried out using a large data set of moderate to large earthquakes to learn the polarity-picking problem in general. The second stage employed microearthquake data for re-training the model. This reflected a fine-tuning approach (Girshick et al. 2014) during which all the

parameters were optimized in both stages. The merit of this two-stage approach will be illustrated later by the results of the training.

2.3. Data

In the first stage, the Hi-net data of 18,000 earthquakes with P arrival and polarity data in the Japan Meteorological Agency (JMA) catalog were used. Most of these earthquakes were larger than M 3 (Fig. 3). All the data were then spatially divided into the training and validation data sets (Fig. 4a; Table 1).

In the second stage, the model was trained using the P arrival time and polarity of microearthquakes in the Kanto and Chugoku regions, which were manually picked by Geological Survey of Japan, National Institute of Advanced Industrial Science and Technology (AIST). The Kanto data was also used by Imanishi et al. (2019). The majority of earthquakes in these data sets were smaller than M 3 (Fig. 3). The magnitude–frequency distributions were similar to that of the target data set (see Section 3), which will be introduced later. The spatial distributions of events in the Kanto and Chugoku regions are shown in Figs. 4b and 4c, respectively. The number of seismogram sets and earthquakes is summarized in Table 1.

In both stages, seismograms of the vertical component were used. The seismograms had 256 samples, i.e., 156 samples before and 100 samples after P arrival. The samples were 2.56 s long, as the data was sampled at 100 Hz. Low-frequency noise was removed by applying a high-pass filter at 1 Hz. The initial portion of the P-wave was emphasized by clipping seismograms at a particular threshold. Finally, each seismogram was normalized by its maximum value. Seismograms with amplitudes larger than the clipping threshold were normalized by the clipping threshold.

Furthermore, the data was augmented four times by flipping the seismograms upside down and by using time-shifting. The flipping procedure equalized the number of upward and downward polarity data. The time shift addressed the potential misalignment of data due to uncertainties in the arrival-time picking. Various values of the clipping threshold and the time-shift range were subsequently examined.

2.4. Results

A hundred cases with randomly selected clipping thresholds in the range of 10^{-6} to 10^{-4} m/s and with the half-width of the time-shift ranging 0–30 samples were examined. Note that, since the amplitudes of most of the seismograms were smaller than 10^{-4} m/s, in the case of such a large clipping threshold, seismograms were not clipped and were simply normalized by their maximum values. The results were evaluated based on the loss value for the test data set. The results indicated that the shorter the half-width of the time-shift range, the smaller the loss (Fig. 5a). The clipping threshold did not correlate with the loss value (Fig. 5b).

Hereafter, time-shift was not applied and 10^{-5} m/s was used as the clipping threshold. The neural network model was trained using these values.

The performance of the trained neural network model was quantified based on precision and recall. The precision represented how reliable the model prediction was. By focusing on one of the classes (upward or downward), the precision is defined as:

$$\text{Precision} = \frac{\text{TP}}{\text{TP} + \text{FP}}, \qquad (2)$$

where TP represents a true positive, where the neural network model correctly predicts the designated class, and FP is a fault positive, where the model incorrectly predicts the

designated class. Thus, TP and FP for the upward and downward polarities are:

$$\begin{matrix} \mathrm{TP_{up}} = N_{\mathrm{uu}}, & \mathrm{FP_{up}} = N_{\mathrm{du}}, \\ \mathrm{TP_{down}} = N_{\mathrm{dd}}, & \mathrm{FP_{down}} = N_{\mathrm{ud}}, \end{matrix} \quad (3)$$

where N_{ij} is of class i and predicted as class j, and "u" and "d" indicate the upward and downward polarities, respectively. Here, this study acknowledges that the model predicted the upward and downward polarity only when the confidence scores were larger than the confidence threshold. Otherwise, the model prediction is considered to have been ambiguous.

The recall represents how much data of the designated class is recovered by the neural network model, and is defined as:

$$\mathrm{Recall} = \frac{\mathrm{TP}}{\mathrm{TP} + \mathrm{FN}}, \quad (4)$$

where FN is a false negative, where the model incorrectly predicts the designated class, and

$$\mathrm{FN_{up}} = N_{\mathrm{ud}} + N_{\mathrm{ua}}, \quad \mathrm{FN_{down}} = N_{\mathrm{du}} + N_{\mathrm{da}}, \quad (5)$$

where the subscript "a" indicates ambiguous, where the confidence score is lower than the confidence threshold.

As the precision and the recall are functions of the confidence threshold, a curve of precision and recall can be drawn as shown in Fig. 5c. The better the model performance, the closer to the top right corner the precision-recall curve will be. Comparing the curves for the model trained only by the JMA data set and for the model trained also by the microearthquake data set, the latter showed observably better results. The performances of the models for upward and downward polarities were almost the same.

3. Application to Crustal Earthquakes in Japan

This study applied the trained model to the target data that is event data of earthquakes that occurred in the period 2005–2019 at depths of less than 20 km within the coastline in Japan islands, excluding the events for which polarity information was already available in the JMA catalog (Table 1). The study employed 1,930,132 seismogram sets of 113,700 events from Hi-net and the JMA seismic network, with P-wave arrival times taken from the JMA catalog. The magnitude–frequency distribution of earthquakes analyzed is shown in Fig. 3. Preprocessing was done in the same manner as in the model training. Good results were obtained for polarity picking with high confidence scores (Fig. 6), even in noisy cases.

The focal mechanisms were determined using polarity information with confidence scores larger than a confidence threshold and the HASH code (Hardebeck and Shearer 2002, 2008). The quality of focal mechanisms depended on the confidence threshold (Fig. 5d). If the threshold was too high, the very small number of polarity picks could not properly constrain focal mechanisms. If the threshold was lower than 0.7, the fraction of A and B ranks given by the HASH code (Hardebeck and Shearer 2008) was almost constant. This study adopted a confidence threshold of 0.7 and, accordingly, 1,800,937 polarity picks were used.

Fig. 7 shows the estimated focal mechanisms and their P- and T-axes, in addition to the NIED F-net moment tensor solutions for reference. The focal mechanisms of 113,700 events were estimated, while those of 7,313 events were undetermined because the number of seismic stations was smaller than eight. Ranks A, B, C, and D, given by the HASH code (Hardebeck and Shearer 2008), were assigned to 1,067, 17,897, 36,749, and

50,674 events, respectively. The focal mechanism solutions covered much more space than those in a routine catalog.

4. Discussion

4.1. Quality of the First-motion Polarity Picking and Focal Mechanism Solutions

Somewhat surprisingly, the narrower the time-shift range of the data, the better the model performed (Fig. 5a). This was because the time-shifting made the model more flexible and robust to uncertainties in arrival-time picking. There were two potential reasons for this; one was that the arrival times in the test data were accurate because of careful review by an analyst, and, accordingly, the time-shift was not required. Another possible reason was that the training was not sufficient due to the shortage of microearthquake training data.

The stability of the performance of the trained model was measured by, in addition to the test data set, a comparison of the confidence scores for similar seismic data. First, using a repeating earthquake catalog (Igarashi 2020), 1,673 repeating earthquake pairs were taken. For each event pair, seismogram pairs from identical stations were included. In total, 22,956 pairs of seismograms were selected. Next, the confidence scores of the pairs were compared using the product of the modified confidence scores as a measure of similarity, where the modified confidence score was 2 × (confidence score of the upward polarity – 0.5), to establish their range from −1 to 1. The histogram of the products is shown in Fig. 8. Most of the products were close to 1, which meant a high similarity for the outcome of the trained model. Some cases were close to −1. Examples of the seismograms in such cases are shown in Fig. 9, where some had noticeable opposite

polarities, while others may have been affected by noise. This investigation suggested that the model worked well in most cases, although room for improvement remains.

Determination of focal mechanisms from the first-motion polarities of P-waves picked by the trained neural network model was also important for assessing the quality of polarity picking. In this study, 47.6% of the focal mechanism solutions were ranked D or "undetermined". In a study on the determination of the focal mechanisms of earthquakes in Southern California using manually picked P-wave polarity and the amplitude ratio of P and S waves (Yang et al. 2012), the results showed that 56.6% (101,309 among 178,899) of events were ranked D, comparable to the result of the present study. Thus, the present study yielded a reasonable quality of P-wave first-motion polarity picking; however, based on several factors, this comparison is not entirely straightforward. These factors include differences in observational conditions such as the magnitude range and station density. Focal mechanism determination can be improved in several ways, e.g., by the introduction of P-wave amplitude (e.g., Matsushita and Imanishi 2015; Pugh *et al.* 2016b) and the ratio of P- and S-wave amplitudes (Hardebeck and Shearer 2003; Yang *et al.* 2012), alongside the application of advances in P-wave polarity picking.

The quality of the focal mechanism solutions is shown by region in Fig. 5e. In particular, the quality in the Hokkaido region was much worse than in other regions. The reason for this was examined by focusing on the number of stations. First, the quality of the focal mechanism solutions showed a good correlation with the number of stations (Fig. 5f). Next, the number of usable stations was smaller in Hokkaido than in other regions. This was likely because of the spatial density of seismic stations (Fig. 7e). Hence, it was more difficult to determine the focal mechanisms in Hokkaido than elsewhere.

4.2. Implications for the Stress Field

The spatial distribution of the P- and T-axis azimuths (Figs. 7c and 7d) suggested the placement of crustal stress field in the Japanese islands. In this regard, first the consistency of this study using the F-net catalog on a large scale is confirmed, before briefly discussing the advantages of this study, particularly at small spatiotemporal scales.

The overall features in the spatial distributions of the P- and T-axis azimuths from this study and the F-net catalog were similar. Note that the events investigated by this study and those included in the F-net catalog were largely different, as implied by the different magnitude distributions (Fig. 3). Accordingly, an overview of the spatial trend is provided by introducing two parameters from directional statistics, i.e., mean direction and circular standard deviation (CSD) (e.g., Ley and Verdebout 2017). The mean direction of directional data $(\theta_1, \theta_2, \ldots, \theta_N)$ is defined as $\bar{\theta}$, which satisfies the following equations:

$$\cos\bar{\theta} = \bar{C} = \frac{1}{N}\sum_{i=1}^{N}\cos\theta_i, \qquad \sin\bar{\theta} = \bar{S} = \frac{1}{N}\sum_{i=1}^{N}\sin\theta_i. \quad (6)$$

The CSD, V, in the radian is defined as:

$$V = (-2\ln\bar{R})^{1/2} \quad (7)$$

where the mean resultant length, $\bar{R}$, is:

$$\bar{R} = \sqrt{\bar{C}^2 + \bar{S}^2} \quad (8)$$

The mean directions of P- and T-axis azimuths from this study and the F-net catalog at 0.5-degree grids are shown in Fig. 10. The differences in the mean directions from this study and those in the F-net catalog were ~7°–8°, which were within the CSD (~24°) of the present study and thus not significant. No spatial trends were observed in the

differences. Interestingly, the CSD of the P- and T-axes mean directions were systematically larger in the northeast Japan than in the southwest Japan. This was likely because of actual variation in the axes, rather than uncertainty in the focal mechanism determination because the qualities of the focal mechanism solutions did not include such a trend (Fig. 5e).

In the Chugoku region, the P-axes struck in the east–west direction in the northern area (San-in area), whereas those that struck in the northwest–southeast direction did so in the southern area (Sanyo area). The contrast between P-axes azimuths in western Tottori was reported by Kawanishi et al. (2009). The present study also indicated a similar trend for the entire Chugoku region. This contrast geographically corresponded to the San-in shear zone (Meneses-Gutierrez and Nishimura 2020). A combination of the current study alongside geodetic implications will further help to enhance an understanding of seismotectonics.

Local abnormal stress fields can be detected by focal mechanisms. In the Kansai region (Fig. 11), the majority of earthquakes exhibited east–west striking P-axes and north–south T-axes, while groups of events with different trends were also observed, i.e., one group of normal faulting events with P-axes in the north–south direction, and another group of events with northeast–southwest P-axes and northwest–southeast T-axes. Knowing the origins of such local stresses will be helpful to tectonic studies.

Rich focal mechanism data will also assist the study of temporal changes in the stress field. Fig. 12 shows the orientations of the T-axes before and after the 2016 Kumamoto earthquake in central Kyushu. T-axes tend to be in the north–south direction, as indicated by existing studies (e.g., Matsumoto *et al.* 2015; Savage *et al.* 2016). Small changes in

297 the T-axes azimuths at the 2016 Kumamoto earthquake may have been due to, e.g., the
298 stress rotation effected by large foreshocks and the mainshock (Yoshida et al. 2016), or
299 as a result of different fault geometries. Additional investigation is needed in this regard.

300 Following the 2011 Tohoku-oki earthquake, several events occurred with T-axes in the
301 east–west direction along the Pacific coast of the Kanto and Tohoku regions, whereas the
302 majority of events in the entire Kanto and Tohoku regions had P-axes in this direction.
303 This seismicity was activated following the 2011 Tohoku-oki earthquake. The focal
304 mechanisms of microearthquakes prior to the 2011 Tohoku-oki earthquake were similar
305 to those following the same earthquake in the northern Ibaraki prefecture, the Fukushima
306 Hamadori area (Imanishi *et al.* 2012; Otsubo *et al.* 2018), and the Kitakami mountain
307 range (Yoshida et al. 2015). In the present study, the small number of focal mechanisms
308 in the Boso peninsula before the Tohoku-oki earthquake were similar to those after this
309 earthquake (Fig. 13). The east–west extensional stress field in these areas may have
310 existed before the 2011 Tohoku-oki earthquake.

311 Despite the dramatic increase in focal mechanism solutions, there remain unstudied
312 areas among the Japanese islands, where seismicity is relatively low. Accordingly, this
313 type of study may be required for even smaller earthquakes, a more complex challenge
314 than that addressed in the present study. Additional campaign seismic observations may
315 improve the focal mechanism solutions for very small earthquakes. Furthermore,
316 combining these observations with research that includes geological, geographical, and
317 geodetical observations will improve our understanding of the crustal stress field and its
318 origin.

5. Conclusions

In this study, the focal mechanisms of small to microearthquakes were estimated for gaining a better understanding of the crustal stress fields in the area of the Japanese islands. The focal mechanisms were derived using P-wave first-motion polarities, picked by a neural network model that takes the vertical component of seismograms with P arrival times as input. The focal mechanisms of almost all microearthquakes in the entire area of the Japanese islands were successfully determined. The focal mechanism solutions were generally consistent with the stress regime on a large scale. For example, the slight but observable differences in the P-axis azimuths in the northern and southern parts of the Chugoku region were consistent with the geodetic observations for this region. The results of this study will be useful for revealing the crustal stress field, and, accordingly, for assessing past and current tectonic activities and future earthquake generation.

Acknowledgements

I thank Kazutoshi Imanishi and Reiken Matsushita for providing phase data for microearthquakes in Kanto and Chugoku regions in Japan. I also thank the NIED, especially Takanori Matsuzawa, for helping me prepare the large seismic data set. Careful reviews and constructive comments by the Editor Eiichi Fukuyama and two anonymous reviewers improved this paper. I used seismic data from NIED Hi-net (National Research Institute for Earth Science and Disaster Resilience 2020) and JMA available at http://www.hinet.bosai.go.jp/?LANG=en (last accessed on 25 June 2020), the phase data from the JMA Unified Earthquake Catalog, available at http://www.data.jma.go.jp/svd/eqev/data/bulletin/eqdoc_e.html (last accessed on 25 June 2020) and http://www.hinet.bosai.go.jp/?LANG=en (last accessed on 25 June 2020), and

the moment tensor solutions by NIED F-net project (Fukuyama et al. 1998) available at http://www.fnet.bosai.go.jp/top.php?LANG=en (last accessed on 25 June 2020). The data analyses in this study were performed using PyTorch (Paszke et al. 2019), ObsPy (Beyreuther *et al.* 2010; Megies *et al.* 2011; Krischer *et al.* 2015), HASH (Hardebeck and Shearer 2002, 2008), and HASHpy (Williams 2014). I used Generic Mapping Tools (Wessel et al. 2013) for generating Figs. 3, 4, 5, 7, 10, 11, 12, and 13, and Matplotlib (Hunter 2007) for Figs. 2, 6, 8, and 9. This work was supported by Mitsubishi Foundation and AIST EDGE Runners project. In this work, the computation facility of the AI Bridging Cloud Infrastructure (ABCI) maintained by AIST was employed.

References

Amante, C. & Eakins, B.W., 2009. ETOPO1 1 Arc-Minute Global Relief Model: Procedures, Data Sources and Analysis. *in NOAA Technical Memorandum NESDIS NGDC-24* National Geophysical Data Center, NOAA, doi:10.7289/V5C8276M.

Beyreuther, M., Barsch, R., Krischer, L., Megies, T., Behr, Y. & Wassermann, J., 2010. ObsPy: A Python Toolbox for Seismology, *Seismol. Res. Lett.,* 81**,** 530-533, doi:10.1785/gssrl.81.3.530.

Brodsky, E.E., Saffer, D., Fulton, P., Chester, F., Conin, M., Huffman, K., Moore, J.C. & Wu, H.-Y., 2017. The postearthquake stress state on the Tohoku megathrust as constrained by reanalysis of the JFAST breakout data, *Geophys. Res. Lett.,* 44**,** 8294-8302, doi:10.1002/2017GL074027.

Chen, C. & Holland, A.A., 2016. PhasePApy: A Robust Pure Python Package for Automatic Identification of Seismic Phases, *Seismol. Res. Lett.,* 87**,** 1384-1396,

365 doi:10.1785/0220160019.

366 Dreger, D.S. & Helmberger, D.V., 1993. Determination of source parameters at regional
367 distances with three-component sparse network data, *J. Geophys. Res.,* 98**,** 8107-
368 8125, doi:10.1029/93JB00023.

369 Ekström, G., Nettles, M. & Dziewoński, A.M., 2012. The global CMT project 2004–
370 2010: Centroid-moment tensors for 13,017 earthquakes, *Phys. Earth Plant. Inter.,*
371 200–201**,** 1-9, doi:10.1016/j.pepi.2012.04.002.

372 Fukuyama, E., Ishida, M., Dreger, D.S. & Kawai, H., 1998. Automated seismic moment
373 tensor determination by using on-line broadband seismic waveforms, *Zisin 2nd*
374 *Ser.,* 51**,** 149-156, doi:10.4294/zisin1948.51.1_149. (*in Japanese with English*
375 *abstract*)

376 Girshick, R., Donahue, J., Darrell, T. & Malik, J., 2014. Rich Feature Hierarchies for
377 Accurate Object Detection and Semantic Segmentation. *in 2014 IEEE Conference*
378 *on Computer Vision and Pattern Recognition*, pp. 580-587,
379 doi:10.1109/CVPR.2014.81.

380 Hara, S., Fukahata, Y. & Iio, Y., 2019. P-wave first-motion polarity determination of
381 waveform data in western Japan using deep learning, *Earth Planets Space,* 71**,**
382 127, doi:10.1186/s40623-019-1111-x.

383 Hardebeck, J.L., 2015. Stress orientations in subduction zones and the strength of
384 subduction megathrust faults, *Science,* 349**,** 1213-1216,
385 doi:10.1126/science.aac5625.

386 Hardebeck, J.L. & Shearer, P.M., 2002. A new method for determining first-motion focal
387 mechanisms, *Bull. Seismol. Soc. Am.,* 92**,** 2264-2276, doi:10.1785/0120010200.

388 Hardebeck, J.L. & Shearer, P.M., 2003. Using S/P amplitude ratios to constrain the focal

mechanisms of small earthquakes, *Bull. Seismol. Soc. Am.,* 93**,** 2434-2444, doi:10.1785/0120020236.

Hardebeck, J.L. & Shearer, P.M., 2008. HASH: A FORTRAN program for computing earthquake first-motion focal mechanisms – v1.2 –.

Heidbach, O., Rajabi, M., Cui, X., Fuchs, K., Müller, B., Reinecker, J., Reiter, K., Tingay, M., Wenzel, F., Xie, F., Ziegler, M.O., Zoback, M.-L. & Zoback, M., 2018. The World Stress Map database release 2016: Crustal stress pattern across scales, *Tectonophysics,* 744**,** 484-498, doi:10.1016/j.tecto.2018.07.007.

Heidbach, O., Rajabi, M., Reiter, K., Ziegler, M. & Team, W., 2016. World Stress Map Database Release 2016. *in GFZ Data Services*, doi:10.5880/WSM.2016.001.

Heidbach, O., Tingay, M., Barth, A., Reinecker, J., Kurfeß, D. & Müller, B., 2008. The World Stress Map database release 2008, doi:10.1594/GFZ.WSM.Rel2008.

Hornik, K., 1991. Approximation capabilities of multilayer feedforward networks, *Neural Networks,* 4**,** 251-257, doi:10.1016/0893-6080(91)90009-T.

Huffman, K.A., Saffer, D.M. & Dugan, B., 2016. In situ stress magnitude and rock strength in the Nankai accretionary complex: a novel approach using paired constraints from downhole data in two wells, *Earth Planets Space,* 68**,** 123, doi:10.1186/s40623-016-0491-4.

Hunter, J.D., 2007. Matplotlib: A 2D Graphics Environment, *Comput. Sci. Eng.,* 9**,** 90-95, doi:10.1109/MCSE.2007.55.

Igarashi, T., 2020. Catalog of small repeating earthquakes for the Japanese Islands, *Earth Planets Space,* 72**,** 73, doi:10.1186/s40623-020-01205-2.

Iio, Y., Kishimoto, S., Nakao, S., Miura, T., Yoneda, I., Sawada, M. & Katao, H., 2018. Extremely weak fault planes: An estimate of focal mechanisms from stationary

seismic activity in the San'in district, Japan, *Tectonophysics,* 723**,** 136-148, doi:10.1016/j.tecto.2017.12.007.

Imanishi, K., Ando, R. & Kuwahara, Y., 2012. Unusual shallow normal-faulting earthquake sequence in compressional northeast Japan activated after the 2011 off the Pacific coast of Tohoku earthquake, *Geophys. Res. Lett.,* 39**,** L09306, doi:10.1029/2012GL051491.

Imanishi, K., Kuwahara, Y., Takeda, T., Mizuno, T., Ito, H., Ito, K., Wada, H. & Haryu, Y., 2011. Depth-dependent stress field in and around the Atotsugawa fault, central Japan, deduced from microearthquake focal mechanisms: Evidence for localized aseismic deformation in the downward extension of the fault, *J. Geophys. Res.,* 116**,** B01305, doi:10.1029/2010JB007900.

Imanishi, K., Uchide, T., Ohtani, M., Matsushita, R. & Nakai, M., 2019. Construction of the crustal stress map in the Kanto region, central Japan, *Bull. Geol. Surv. Jpn.,* 70**,** 273-298. (*in Japanese with English abstract*)

Ioffe, S. & Szegedy, C., 2015. Batch normalization: accelerating deep network training by reducing internal covariate shift. *in ArXiv e-prints*.

Kawanishi, R., Iio, Y., Yukutake, Y., Shibutani, T. & Katao, H., 2009. Local stress concentration in the seismic belt along the Japan Sea coast inferred from precise focal mechanisms: Implications for the stress accumulation process on intraplate earthquake faults, *J. Geophys. Res. Solid Earth,* 114, doi:10.1029/2008jb005765.

Kingma, D.P. & Ba, J., 2014. Adam: A method for stochastic optimization, *arXiv preprint arXiv:1412.6980*.

Krischer, L., Megies, T., Barsch, R., Beyreuther, M., Lecocq, T., Caudron, C. & Wassermann, J., 2015. ObsPy: a bridge for seismology into the scientific Python

437 ecosystem, *Comput. Sci. Discov.,* 8, doi:10.1088/1749-4699/8/1/014003.
438 Ley, C. & Verdebout, T., 2017. *Modern directional statistics*, pp. 190, CRC Press, New
439 York, doi:10.1201/9781315119472.
440 Matsumoto, S., Nakao, S., Ohkura, T., Miyazaki, M., Shimizu, H., Abe, Y., Inoue, H.,
441 Nakamoto, M., Yoshikawa, S. & Yamashita, Y., 2015. Spatial heterogeneities in
442 tectonic stress in Kyushu, Japan and their relation to a major shear zone, *Earth*
443 *Planets Space,* 67**,** 172, doi:10.1186/s40623-015-0342-8.
444 Matsushita, R. & Imanishi, K., 2015. Stress fields in and around metropolitan Osaka,
445 Japan, deduced from microearthquake focal mechanisms, *Tectonophysics,* 642**,**
446 46-57, doi:10.1016/j.tecto.2014.12.011.
447 Megies, T., Beyreuther, M., Barsch, R., Krischer, L. & Wassermann, J., 2011. ObsPy –
448 What can it do for data centers and observatories?, *Ann. Geophys.,* 54**,** 12,
449 doi:10.4401/ag-4838.
450 Meneses-Gutierrez, A. & Nishimura, T., 2020. Inelastic deformation zone in the lower
451 crust for the San-in Shear Zone, Southwest Japan, as observed by a dense GNSS
452 network, *Earth Planets Space,* 72**,** 10, doi:10.1186/s40623-020-1138-z.
453 Nair, V. & Hinton, G.E., 2010. Rectified linear units improve restricted boltzmann
454 machines. *in 27th International Conference on Machine Learning (ICML-10)*, pp.
455 807-814, Haifa, Israel.
456 Nakamura, M., 2004. Automatic determination of focal mechanism solutions using initial
457 motion polarities of P and S waves, *Phys. Earth Plant. Inter.,* 146**,** 531-549,
458 doi:10.1016/j.pepi.2004.05.009.
459 National Research Institute for Earth Science and Disaster Resilience, 2020. NIED Hi-
460 net, National Research Institute for Earth Science and Disaster Resilience.

doi:10.17598/NIED.0003.

Otsubo, M., Miyakawa, A. & Imanishi, K., 2018. Normal-faulting stress state associated with low differential stress in an overriding plate in northeast Japan prior to the 2011 Mw 9.0 Tohoku earthquake, *Earth Planets Space,* 70, doi:10.1186/s40623-018-0813-9.

Paszke, A., Gross, S., Massa, F., Lerer, A., Bradbury, J., Chanan, G., Killeen, T., Lin, Z., Gimelshein, N., Antiga, L., Desmaison, A., Kopf, A., Yang, E., DeVito, Z., Raison, M., Tejani, A., Chilamkurthy, S., Steiner, B., Fang, L., Bai, J. & Chintala, S., 2019. PyTorch: An imperative style, high-performance deep learning library. *in Advances in Neural Information Processing Systems*, pp. 8024-8035, Curran Associates, Inc.

Pugh, D.J., White, R.S. & Christie, P.A.F., 2016a. Automatic Bayesian polarity determination, *Geophys. J. Int.,* 206**,** 275-291, doi:10.1093/gji/ggw146.

Pugh, D.J., White, R.S. & Christie, P.A.F., 2016b. A Bayesian method for microseismic source inversion, *Geophys. J. Int.*, doi:10.1093/gji/ggw186.

Ross, Z.E., Meier, M.-A. & Hauksson, E., 2018. P wave arrival picking and first-motion polarity determination with deep learning, *J. Geophys. Res. Solid Earth,* 123**,** 5120-5129, doi:10.1029/2017JB015251.

Rumelhart, D.E., Hinton, G.E. & Williams, R.J., 1986. Learning representations by back-propagating errors, *Nature,* 323**,** 533-536, doi:10.1038/323533a0.

Savage, M.K., Aoki, Y., Unglert, K., Ohkura, T., Umakoshi, K., Shimizu, H., Iguchi, M., Tameguri, T., Ohminato, T. & Mori, J., 2016. Stress, strain rate and anisotropy in Kyushu, Japan, *Earth Planet. Sci. Lett.,* 439**,** 129-142, doi:10.1016/j.epsl.2016.01.005.

485 Shearer, P.M., Prieto, G.A. & Hauksson, E., 2006. Comprehensive analysis of earthquake
486 source spectra in Southern California, *J. Geophys. Res.,* 111**,** B06303,
487 doi:10.1029/2005JB003979.
488 Srivastava, N., Hinton, G., Krizhevsky, A., Sutskever, I. & Salakhutdinov, R., 2014.
489 Dropout: a simple way to prevent neural networks from overfitting, *J. Mach.*
490 *Learn. Res.,* 15**,** 1929-1958.
491 Terakawa, T. & Matsu'ura, M., 2010. The 3-D tectonic stress fields in and around Japan
492 inverted from centroid moment tensor data of seismic events, *Tectonics,* 29**,**
493 TC6008, doi:10.1029/2009TC002626.
494 Townend, J., Sutherland, R., Toy, V.G., Doan, M.-L., Célérier, B., Massiot, C., Coussens,
495 J., Jeppson, T., Janku-Capova, L., Remaud, L., Upton, P., Schmitt, D.R., Pezard,
496 P., Williams, J., Allen, M.J., Baratin, L.-M., Barth, N., Becroft, L., Boese, C.M.,
497 Boulton, C., Broderick, N., Carpenter, B., Chamberlain, C.J., Cooper, A., Coutts,
498 A., Cox, S.C., Craw, L., Eccles, J.D., Faulkner, D., Grieve, J., Grochowski, J.,
499 Gulley, A., Hartog, A., Henry, G., Howarth, J., Jacobs, K., Kato, N., Keys, S.,
500 Kirilova, M., Kometani, Y., Langridge, R., Lin, W., Little, T., Lukacs, A., Mallyon,
501 D., Mariani, E., Mathewson, L., Melosh, B., Menzies, C., Moore, J., Morales, L.,
502 Mori, H., Niemeijer, A., Nishikawa, O., Nitsch, O., Paris, J., Prior, D.J., Sauer, K.,
503 Savage, M.K., Schleicher, A., Shigematsu, N., Taylor-Offord, S., Teagle, D.,
504 Tobin, H., Valdez, R., Weaver, K., Wiersberg, T. & Zimmer, M., 2017.
505 Petrophysical, Geochemical, and Hydrological Evidence for Extensive Fracture-
506 Mediated Fluid and Heat Transport in the Alpine Fault's Hanging-Wall Damage
507 Zone, *Geochem. Geophys. Geosyst.,* 18**,** 4709-4732, doi:10.1002/2017GC007202.
508 Wessel, P., Smith, W.H.F., Scharroo, R., Luis, J. & Wobbe, F., 2013. Generic Mapping

509 Tools: Improved Version Released, *EOS,* 94**,** 409-410,
510 doi:10.1002/2013eo450001.
511 Williams, M.C., 2014. HASHpy, doi:10.5281/zenodo.9808.
512 Wu, H.-Y., Ma, K.-F., Zoback, M., Boness, N., Ito, H., Hung, J.-H. & Hickman, S., 2007.
513 Stress orientations of Taiwan Chelungpu-Fault Drilling Project (TCDP) hole-A as
514 observed from geophysical logs, *Geophys. Res. Lett.,* 34,
515 doi:10.1029/2006GL028050.
516 Yang, W., Hauksson, E. & Shearer, P.M., 2012. Computing a large refined catalog of focal
517 mechanisms for southern California (1981–2010): Temporal stability of the style
518 of faulting, *Bull. Seismol. Soc. Am.,* 102**,** 1179-1194, doi:10.1785/0120110311.
519 Yoshida, K., Hasegawa, A. & Okada, T., 2015. Spatial variation of stress orientations in
520 NE Japan revealed by dense seismic observations, *Tectonophysics,* 647–648**,** 63-
521 72, doi:10.1016/j.tecto.2015.02.013.
522 Yoshida, K., Hasegawa, A., Saito, T., Asano, Y., Tanaka, S., Sawazaki, K., Urata, Y. &
523 Fukuyama, E., 2016. Stress rotations due to the M6.5 foreshock and M7.3 main
524 shock in the 2016 Kumamoto, SW Japan, earthquake sequence, *Geophys. Res.*
525 *Lett.,* 43**,** 10097-10104, doi:10.1002/2016GL070581.
526

527

Tables

Table 1

Numbers of seismograms and earthquakes included in the data sets.

Region	Type of Data Set	Seismogram Sets	Earthquakes
Entire Japan	Training	279,483	17,402
	Validation	7,666	598
Kanto	Training	12,814	1,262
	Validation	784	56
	Test	1,483	113
Chugoku	Training	63,359	2,259
	Validation	7,674	322
	Test	12,838	595
Entire Japan	Application	1,930,132	113,700

Figures

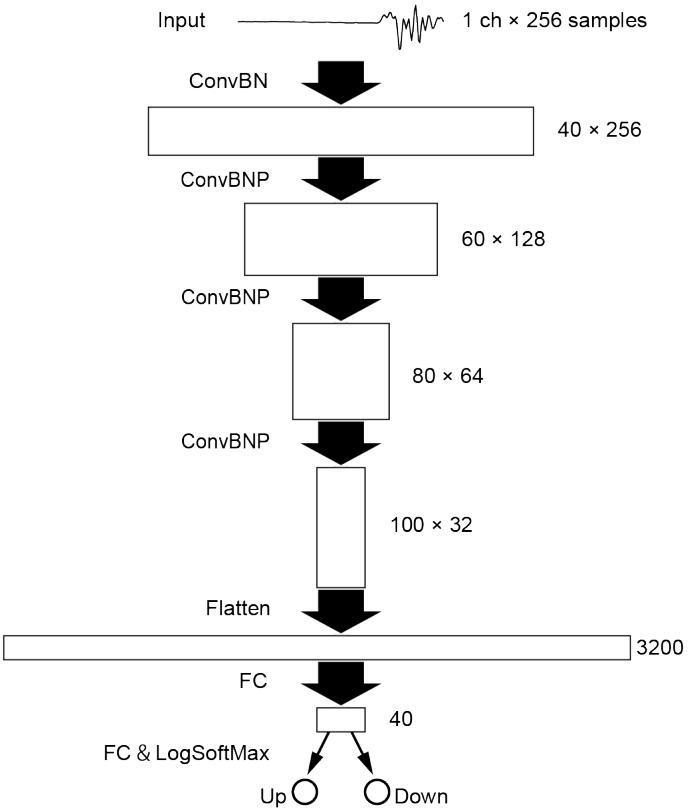

Fig. 1

The design of the neural network model. The numbers on the right indicate the number of channels and samples, while "ConvBN," "Conv BNP," and "FC" denote convolution and batch normalization layers, convolution, batch normalization, and pooling layers, and fully connected layers, respectively.

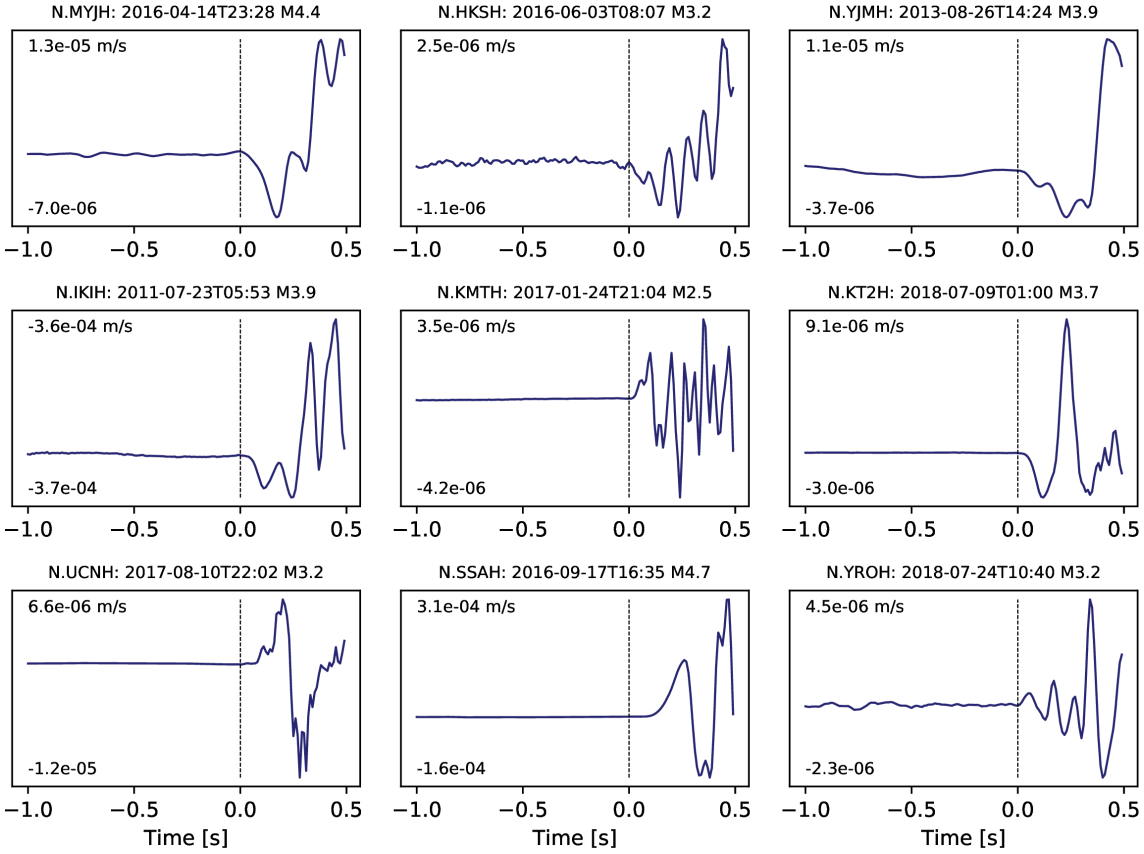

Fig. 2

Examples of seismograms with impulsive onsets but no accompanying polarity data in the JMA Unified Earthquake Catalog. Station names and the origin time and magnitude of the events are indicated above each panel. Note that this data was not used in the study.

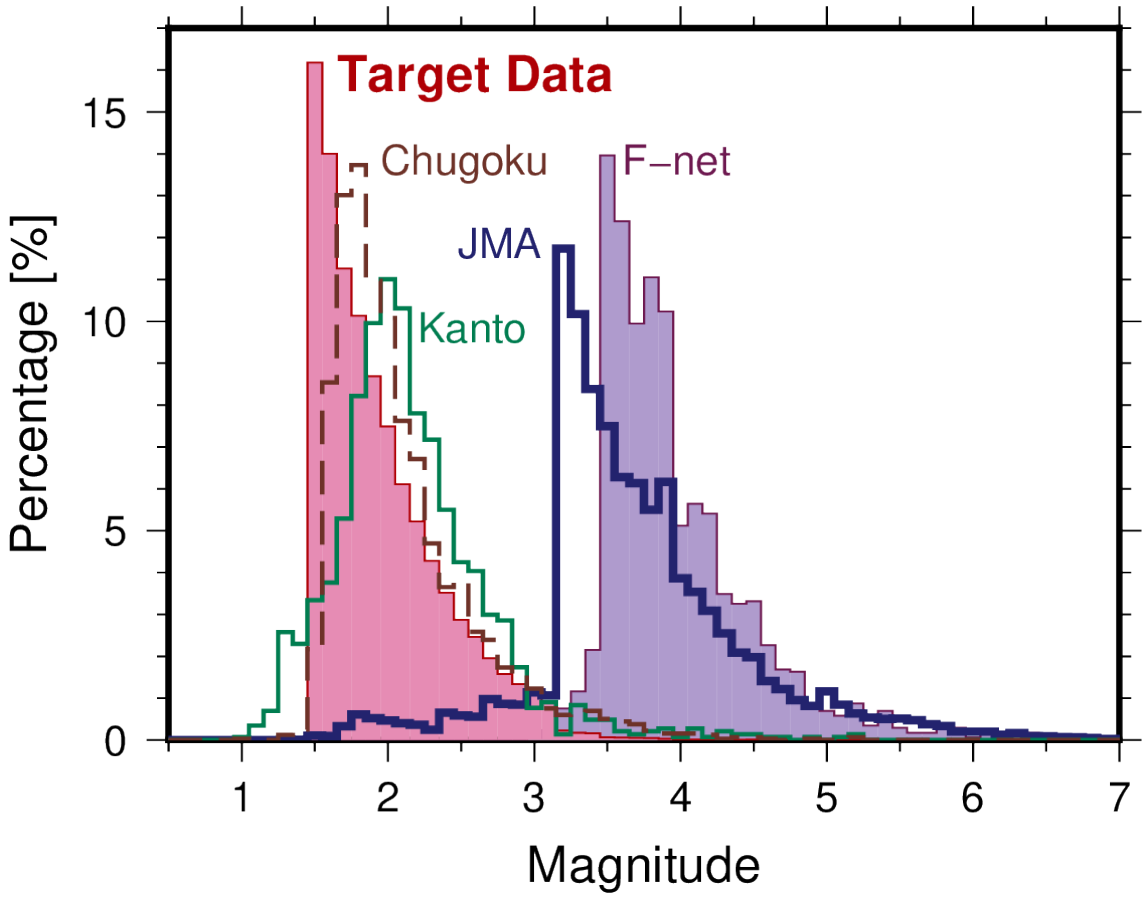

544

545 Fig. 3

546 Magnitude–frequency distributions in the data for the target (pink shade), F-net (purple

547 shade), the JMA (thick navy), Kanto (thin green), and Chugoku (dashed brown) data sets.

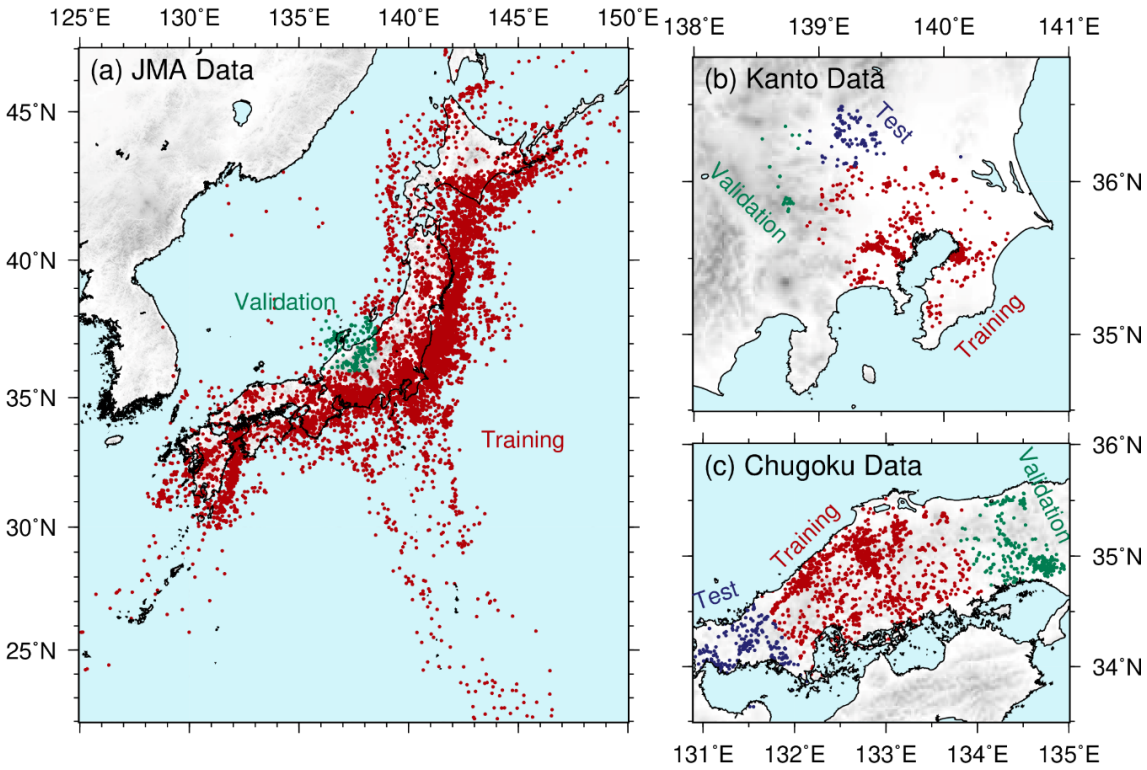

Fig. 4

Distribution of the epicentres of the earthquakes used for training (red), validation (green), and testing (blue) of the neural network model. The topography was taken from ETOPO1 (Amante and Eakins 2009).

553

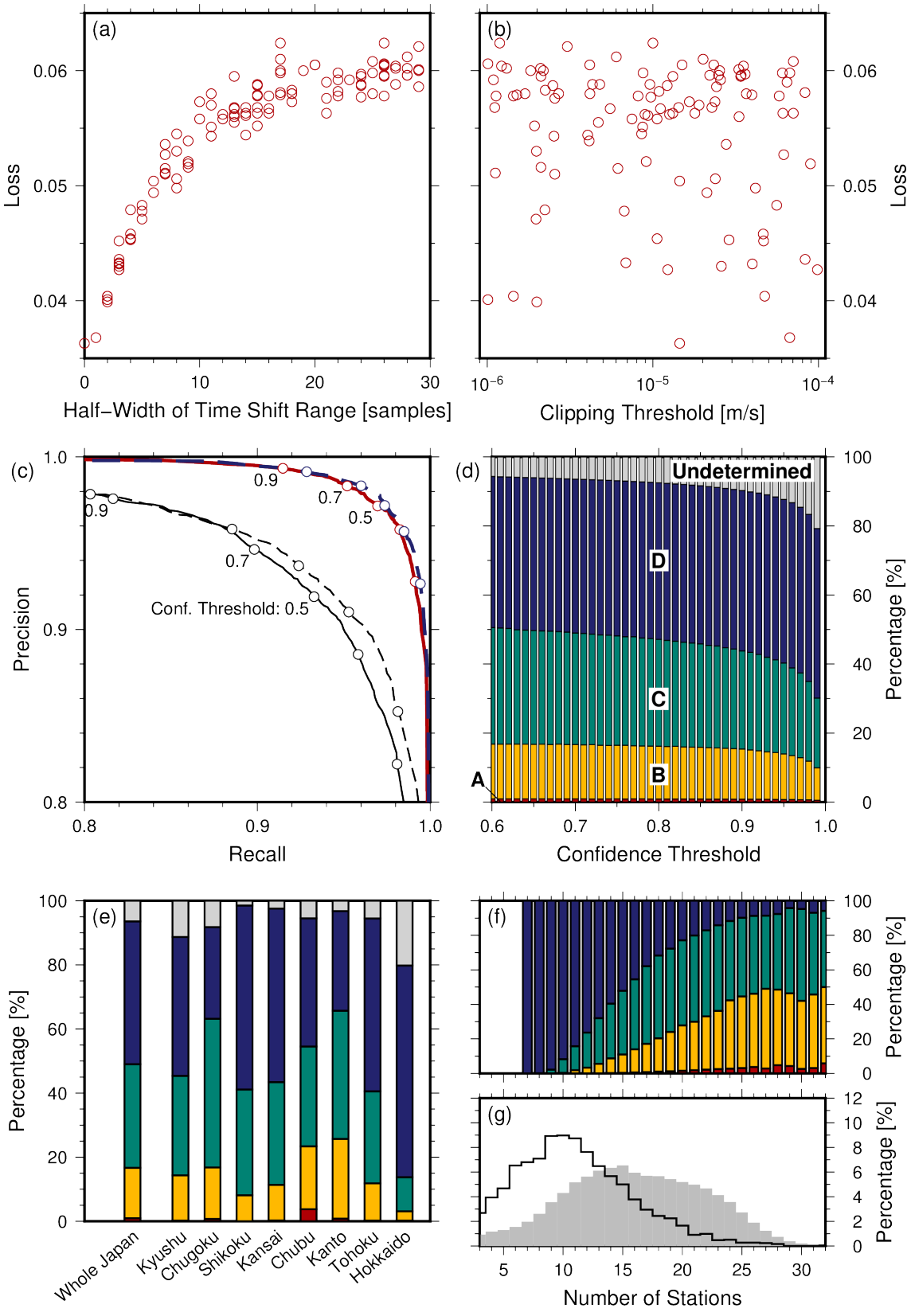
(a)
(b)
Loss
0.06
0.05
0.04
0
10
20
30
Half−Width of Time Shift Range [samples]
10^{-6}
10^{-5}
10^{-4}
Clipping Threshold [m/s]
(c)
Precision
1.0
0.9
0.8
0.9
0.7
0.5
Conf. Threshold: 0.5
Recall
(d)
Undetermined
D
C
B
A
Percentage [%]
Confidence Threshold
(e)
Whole Japan
Kyushu
Chugoku
Shikoku
Kansai
Chubu
Kanto
Tohoku
Hokkaido
(f)
(g)
Number of Stations

554

Fig. 5

Summary of the results. Here, (a) and (b) show the loss function values as functions of the time-shift range and the clipping threshold, respectively. (c) The precision-recall curve of the trained model for the test data set. The thick red solid and blue dashed lines refer to the upward and downward polarities, respectively, in the case of the two-stage training. The thin black solid and dashed lines refer to the upward and downward polarities, respectively, where the model was trained using only the JMA data set. Circles correspond to every 0.1 units of the confidence thresholds. (d) Bar graphs of the rank of the focal mechanism solutions as a function of the confidence threshold. Red, yellow, green, and blue bars from the bottom to the top represent the A, B, C, and D-ranks, respectively. Gray bars on the top indicate undefined focal mechanisms. (e) Bar graphs of the rank of focal mechanism solutions for the whole of Japan and eight specific regions (see Fig. 7e). Here, a model with a confidence threshold of 0.7 was used. The color scheme is the same as in the case of (d). (f) Bar graphs as a function of the number of seismic stations. The color scheme is the same as for (d). (g) Histograms of events as a function of the number of stations. The black line and gray shaded region indicate the values for Hokkaido and other regions, respectively.

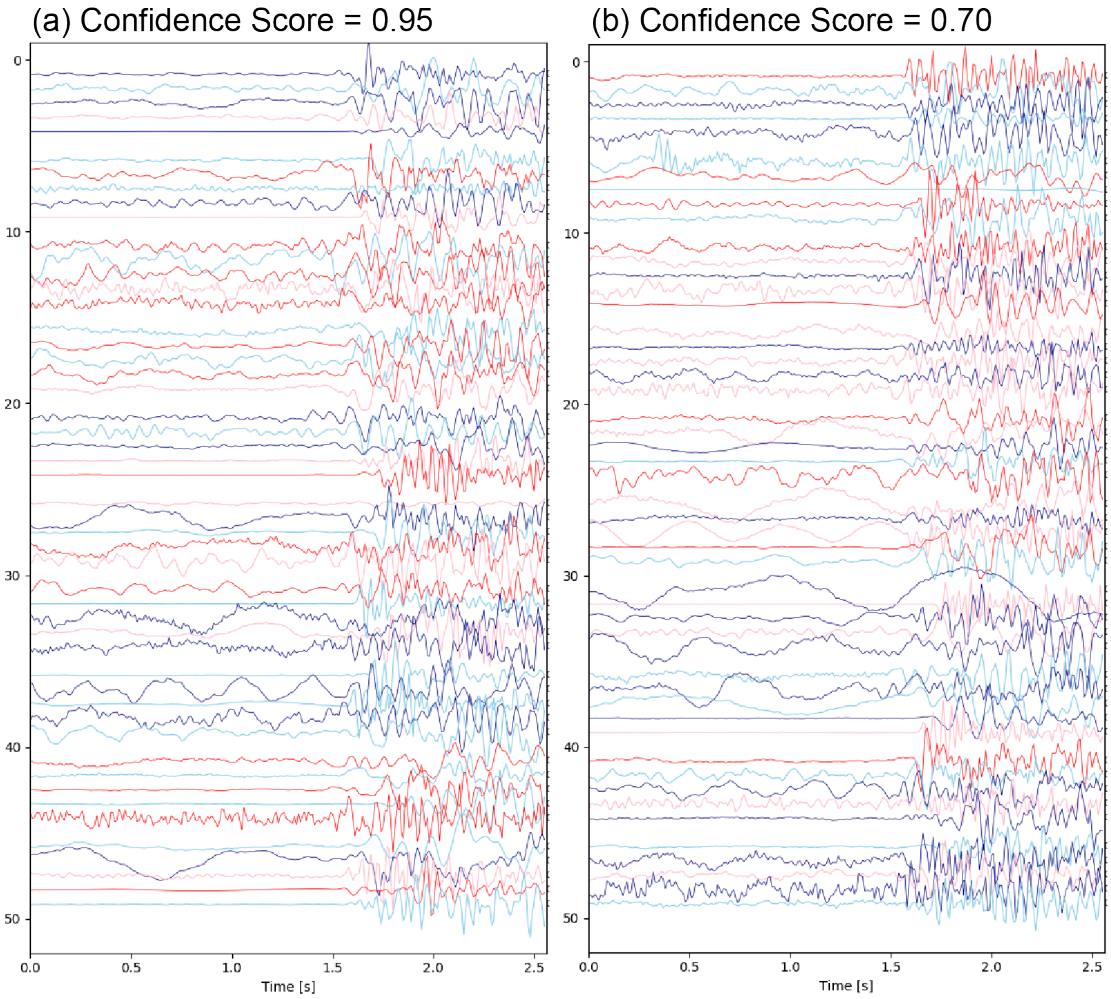

572

573 Fig. 6

574 Examples of seismograms with polarities picked by the neural network model with
575 confidence scores of (a) 0.95 and (b) 0.70. Seismograms with downward polarities are
576 flipped. If correctly picked, the first motion appears upward in this figure. Light and dark
577 colors are alternated for convenience.

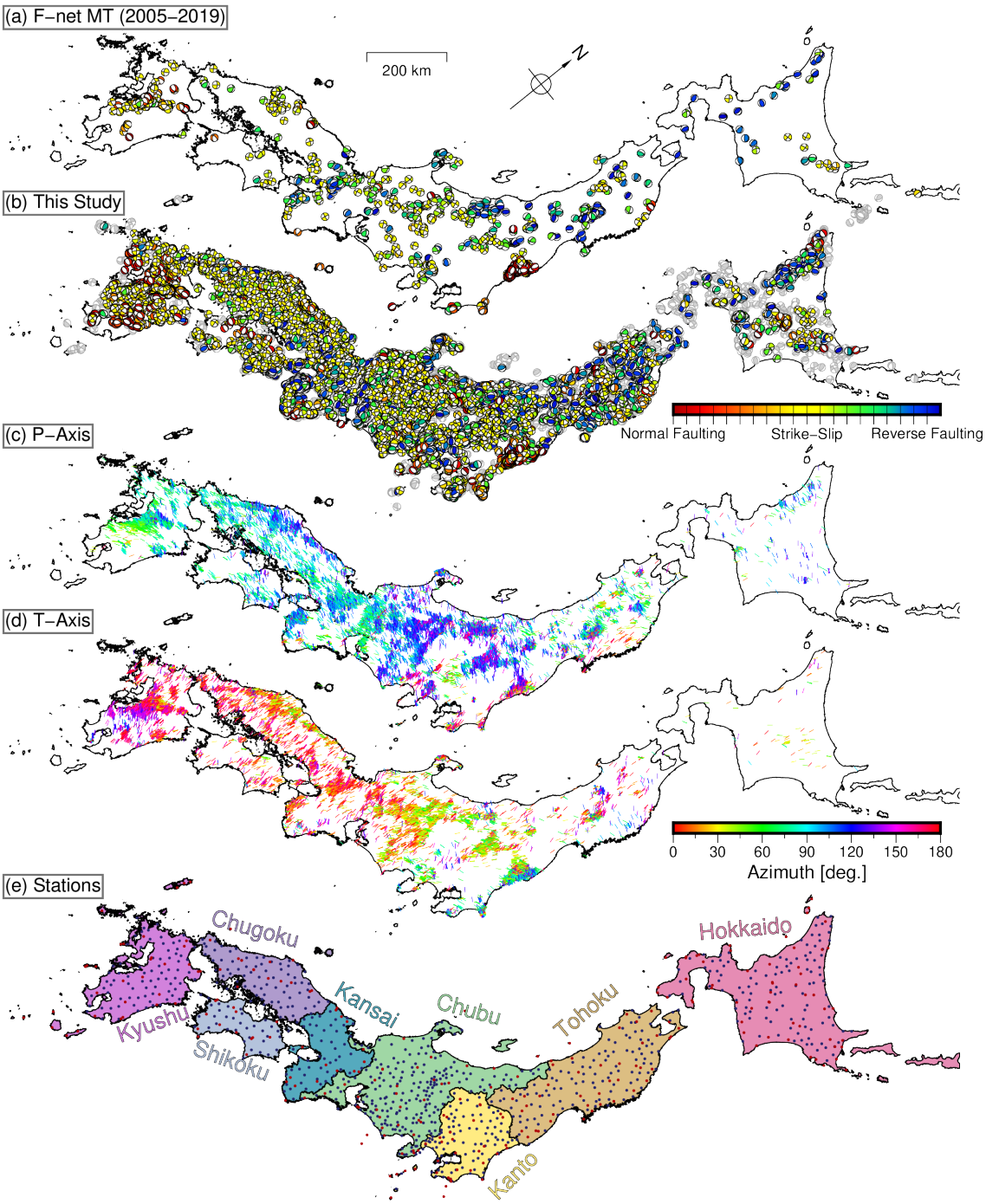

Fig. 7

(a) Moment tensor solutions of earthquakes from 2006–2019 provided by the NIED F-net project (Fukuyama et al. 1998) for reference. (b) Focal mechanism solutions derived by this study. Solutions ranked A–C (Hardebeck and Shearer 2008) are colored according to focal mechanism types (Shearer et al. 2006). The solutions ranked "D" is shown by

584 gray beach balls. (c) Azimuths of the P-axes of the estimated focal mechanism solutions
585 ranked A–C and with plunges less than 30°. Colors indicate the azimuths. (d) Azimuths
586 of the T-axes. (e) Seismic station distribution.

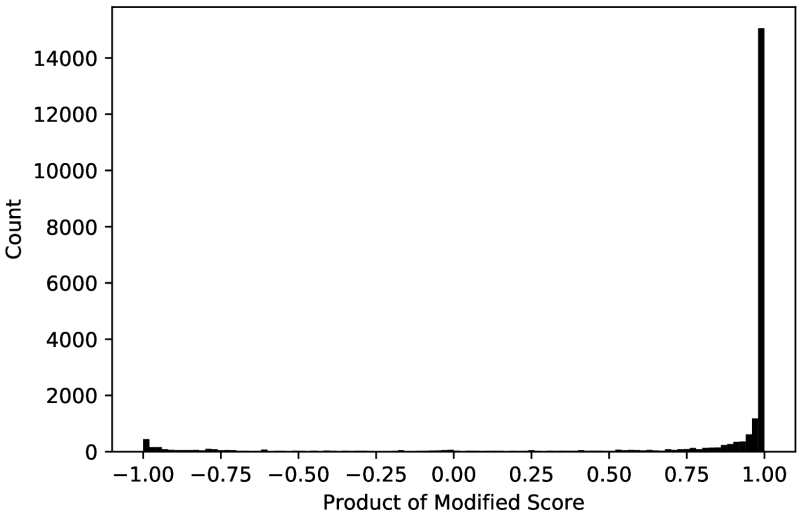

587

588 Fig. 8

589 Histogram of the product of the modified scores of repeating earthquake pairs, where

590 the modified score is 2 × (confidence score for the upward polarity – 0.5).

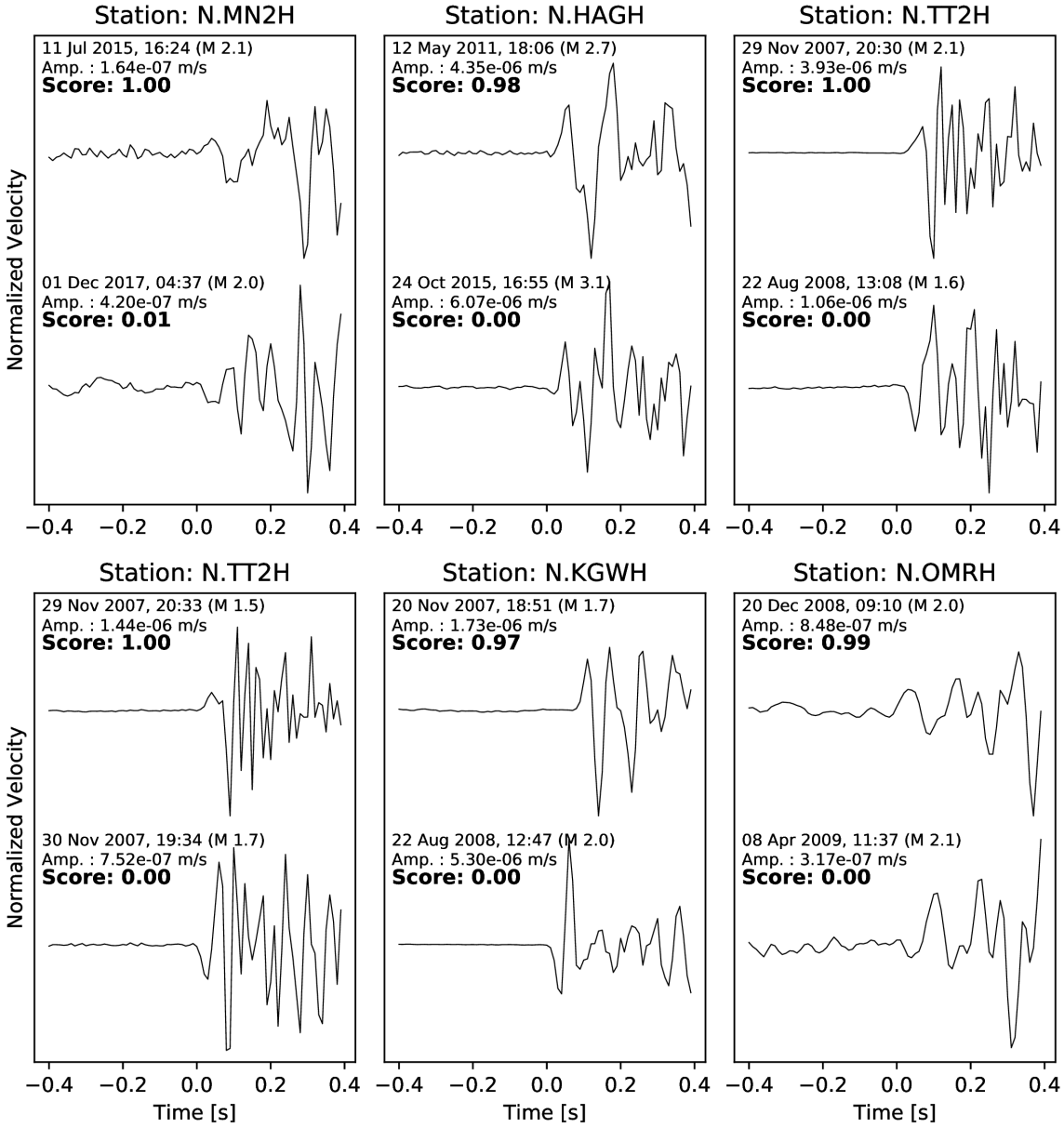

Fig. 9

Comparisons of seismograms of repeating earthquake pairs at the same stations. The scores shown in the panels are the confidence scores for the upward polarity.

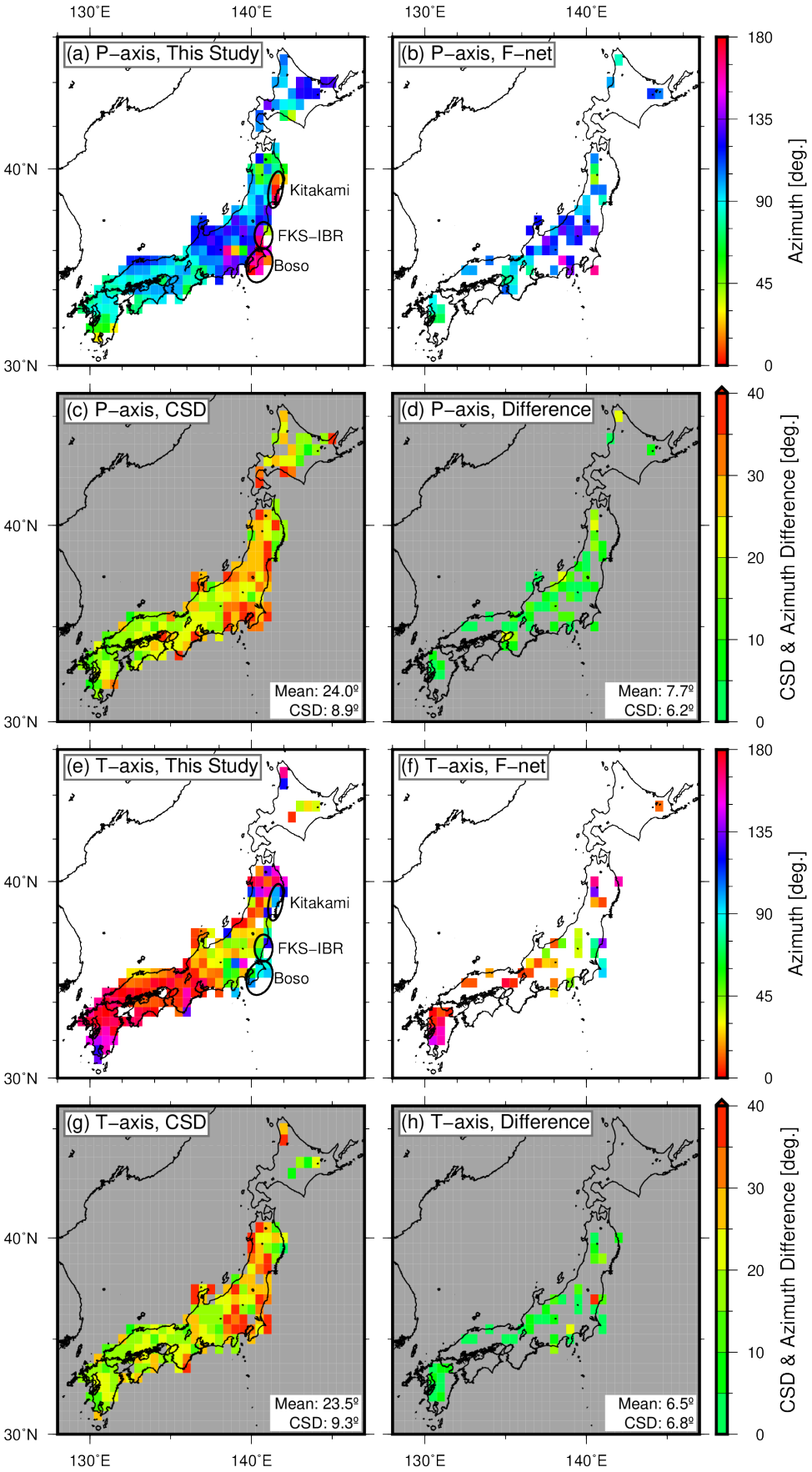
130°E
140°E
(a) P–axis, This Study
(b) P–axis, F–net
(c) P–axis, CSD
(d) P–axis, Difference
(e) T–axis, This Study
(f) T–axis, F–net
(g) T–axis, CSD
(h) T–axis, Difference
40°N
30°N
Kitakami
FKS–IBR
Boso
Mean: 24.0º
CSD: 8.9º
Mean: 7.7º
CSD: 6.2º
Mean: 23.5º
CSD: 9.3º
Mean: 6.5º
CSD: 6.8º
180
135
90
45
0
Azimuth [deg.]
40
30
20
10
0
CSD & Azimuth Difference [deg.]

595

Fig. 10

Spatial distributions of (a) the mean directions of P-axes azimuths from this study and (b) the F-net catalog, (c) the circular standard deviation (CSD) (eq. (7)) of P-axes azimuths from this study, and (d) the absolute values of differences of (a) and (b); (e)–(h) are the values for T-axes. The P- or T- axes with lunges less than 30° and focal mechanism solutions ranked A–C were used. The values at 0.5-degree grids with four or more events are shown. In (a) and (e), the areas in the Kitakami mountain range, Fukushima Hamadori and northern Ibaraki prefecture (FKS-IBR), and Boso peninsula are marked by ellipses.

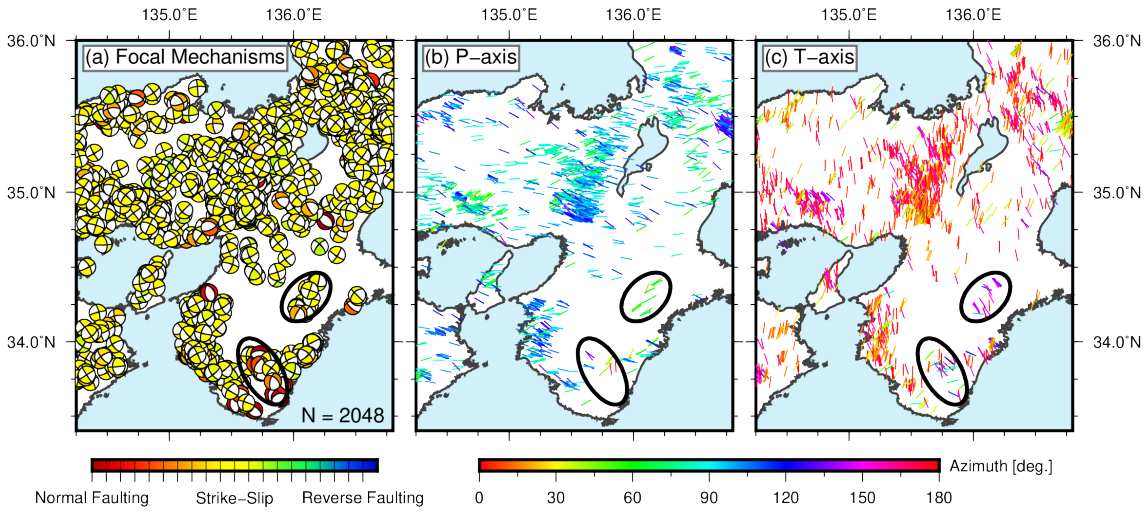

Fig. 11

(a) Focal mechanisms, (b) P-axes, and (c) T-axes in the Kansai area. In (b) and (c), the axes with plunges less than 30° and the focal mechanism solutions ranked A–C were plotted. The ellipses indicate areas with distinct focal mechanisms.

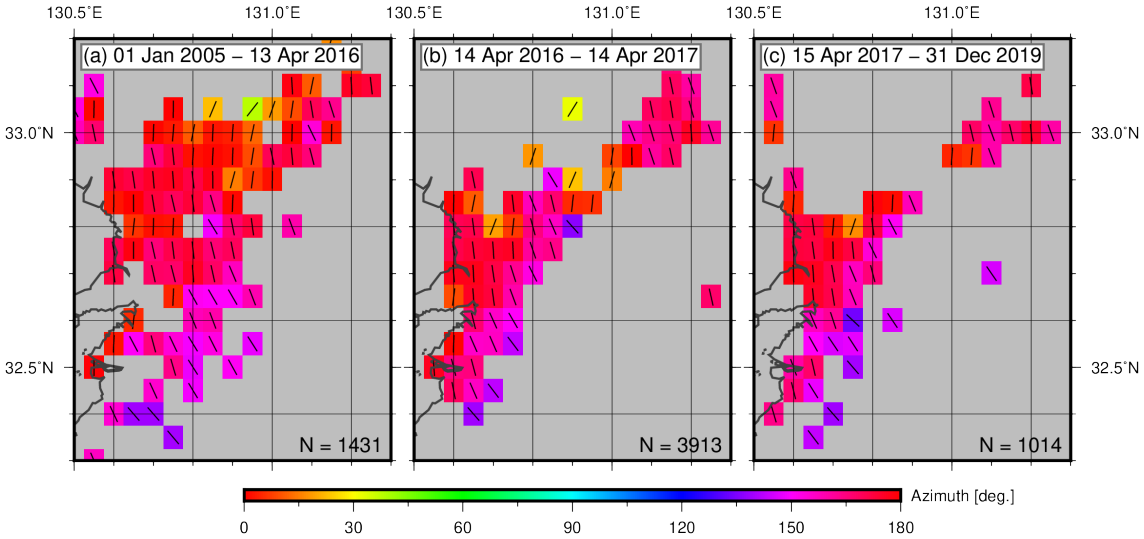

609

610 Fig. 12

611 The mean directions of the T-axes azimuths at 0.05-degree grids (a) before the 2016
612 Kumamoto earthquake, (b) within one year of the Kumamoto earthquake, and (c) after
613 this time, indicated by short bars and colors. T-axes with plunges less than 30° and the
614 focal mechanism solutions ranked A–C were used.

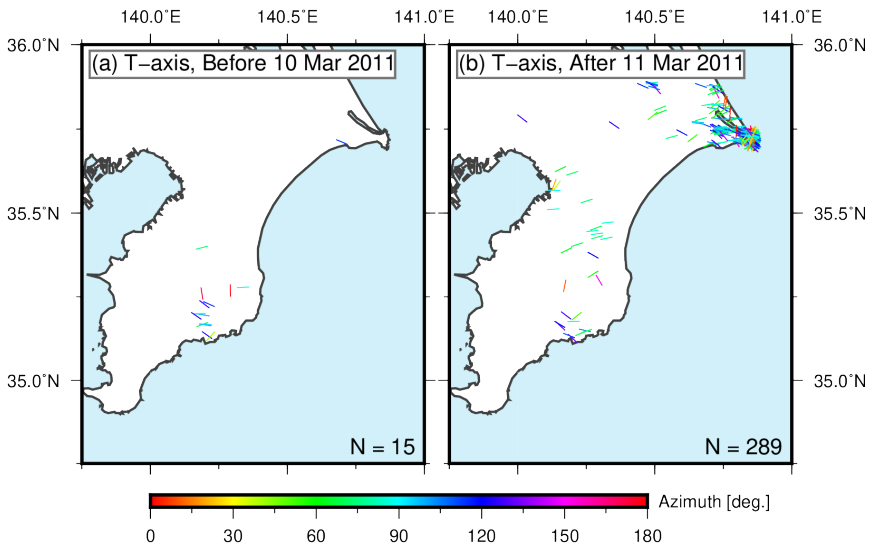

615

616 Fig. 13

617 The T-axis azimuths in the Boso peninsula (a) before and (b) after the 2011 Tohoku-
618 oki earthquake. T-axes with plunges less than 30° and the focal mechanism solutions
619 ranked A–C were plotted.